Dalton Transactions

Accepted Manuscript

ROYAL SOCIETY OF CHEMISTRY

www.rsc.org/dalton

Steric and electronic effects on arylthiolate coordination in the pseudotetrahedral complexes [(Tp^{Ph,Me})Ni–SAr] (Tp^{Ph,Me} = hydrotris{3-phenyl-5-methyl-1-pyrazolyl}borate)†

Tapash Deb,[a] Caitlin M. Anderson,[a] Swarup Chattopadhyay,[a,‡] Huaibo Ma,[a] Victor G. Young, Jr.[b] and Michael P. Jensen[a,*]

[a]*Department of Chemistry and Biochemistry, Ohio University, Athens, Ohio 45701, USA. E-mail: jensenm@ohio.edu*
[b]*X-ray Crystallographic Laboratory, Department of Chemistry, University of Minnesota, Minneapolis, Minnesota 55455, USA.*

ABSTRACT Synthesis and characterization of several new pseudotetrahedral arylthiolate complexes [(Tp^{Ph,Me})Ni–SAr] (Tp^{Ph,Me} = hydrotris{3-phenyl-5-methyl-1-pyrazolyl}borate; Ar = Ph, 2,4,6-^{i}Pr$_3$C$_6$H$_2$, C$_6$H$_4$-4-Cl, C$_6$H$_4$-4-Me, C$_6$H$_4$-4-OMe) are reported, including X-ray crystal structures of the first two complexes. With prior results, two series of complexes are spanned, [(Tp^{Ph,Me})Ni–S–2,4,6-R"$_3$C$_6$H$_2$] (R" = H, Me, ^{i}Pr) plus the xylyl analogue [(Tp^{Ph,Me})Ni–S–2,6-Me$_2$C$_6$H$_3$], as well as [(Tp^{Ph,Me})Ni–S–C$_6$H$_4$-4-Y] (Y = Cl, H, Me, OMe), intended to elucidate steric and/or electronic effects on arylthiolate coordination. In contrast to [(Tp^{Me,Me})Ni–SAr] analogues that adopt a sawhorse conformation, the *ortho*-disubstituted complexes show enhanced trigonal and Ni–S–Ar bending, reflecting the size of the 3-pyrazole substituents. Moreover, weakened scorpionate ligation is implied by spectroscopic data. Little spectroscopic effect is observed in the series of *para*-substituted complexes, suggesting the observed effects are primarily steric in origin. The relatively electron-rich and encumbered complex [(Tp^{Ph,Me})Ni–S–2,4,6-^{i}Pr$_3$C$_6$H$_2$] behaves uniquely when dissolved in CH$_3$CN, forming a square planar solvent adduct with a bidentate scorpionate ligand, [(κ^2-Tp^{Ph,Me})Ni(NCMe)(S–2,4,6-^{i}Pr$_3$C$_6$H$_2$)]. This adduct was isolated and characterized by X-ray crystallography. Single-point DFT and TD-DFT calculations on a simplified [(κ^2-Tp)Ni(NCMe)(SPh)] model were used to clarify the electronic spectrum of the adduct, and to elucidate differences between Ni–SAr bonding and spectroscopy between pseudotetrahedral and square planar geometries.

†Electronic supplementary information (ESI) available: X-ray crystallographic data (.cif); details of the product characterizations and DFT calculations (.pdf). CCDC 1023192–1023194 contain the crystallographic data for this paper. ‡Current address: Department of Chemistry, University of Kalyani, West Bengal, India

1.0. Introduction

The presence of nickel–thiolate bonds in several bacterial enzymes has been revealed by recent structural characterizations, including the active sites of Fe/Ni-hydrogenase, methyl-coenzyme M reductase, acetyl-coenzyme A synthase, and Ni-dependent superoxide dismutases (NiSODs), as well as high-affinity metal binding sites in the accessory protein HypB and the regulatory protein NikR.[1] The diverse array of structures and activities mediated by the thiolate ligands in these proteins provides renewed impetus for exploration of nickel–thiolate chemistry using small-molecule complexes.[2,3] Given the propensity of thiolate ligands to bridge between metals, homoleptic nickel–thiolate complexes are typically polymetallic aggregates;[4] however, monomeric arylthiolate complex dianions $[Ni(SAr)_4]^{2-}$ were characterized,[5–8] as well as a neutral linear species $[Ni(SAr)_2]$ with a very bulky substituent.[9] Monomeric thiolate complexes were also obtained by using a polydentate supporting ligand to circumvent aggregation.[3] Recent work using facially tridentate scorpionate ligands has yielded pseudotetrahedral nickel–thiolate complexes exhibiting rich coordination chemistry and spectroscopy.[10–18]

We have been particularly interested in complexes of hydrotris(3-R–5-Me–pyrazol-1-yl)borates, $[(Tp^{R,Me})Ni–SAr]$ (R = Me, Ph).[15–18] A key feature of the hydrotris(pyrazolyl)borate ligand class is the proximal pocket formed by 3-pyrazole substituents around the binding site for apical co-ligand(s),[19] while the steric bulk and basicity of arylthiolates as co-ligands can be readily manipulated by substitution on the arene ring. We have previously reported associated structural and spectroscopic phenomena elucidated within a series of arylthiolate complexes $[(Tp^{Me,Me})Ni–SAr]$.[15–17] In the present work, $[(Tp^{Ph,Me})Ni–SAr]$ analogues are examined, and the comparison reveals significant steric effects arising from the differing 3-pyrazole substituents.

2.0. Experimental

^{1}H NMR data were recorded on a Varian Unity 500 spectrometer and processed using MestReNova;[20] spectra were referenced internally to residual solvent. Solution magnetic moments were determined by the Evans NMR method in $CDCl_3$ at 295 K.[21] FTIR spectra were obtained from KBr pellets on a Thermo-Electron Nicolet 380 spectrophotometer. UV-Visible-NIR spectra were recorded on an Agilent HP-8453 diode-array spectrophotometer using a jacketed cuvette holder interfaced to a circulating bath equipped with heating and cooling elements under control of a thermostat (VWR). Elemental analyses were performed by Atlantic Microlabs, Inc. (Norcross, GA).

All materials were obtained from commercial vendors as ACS reagent-grade or better and used as received, except for drying of solvents by routine techniques. All manipulations were carried out under an inert atmosphere of prepurified argon, either in a glovebox (MBraun Unilab) or using Schlenk techniques. Syntheses of [(Tp^{Ph,Me})Tl],[22] [(Tp^{Ph,Me})Ni–Cl],[23] NaSAr,[15,16] [(Tp^{Ph,Me})Ni–SPh],[15] [(Tp^{Ph,Me})Ni–S–2,6-$Me_2C_6H_3$][15] and [(Tp^{Ph,Me})Ni–S–2,4,6-$Me_3C_6H_2$][15] were previously described (***caution****: thallium salts are extremely toxic and must be properly handled and disposed of !*).

2.1. Synthesis and characterization of [(Tp^{Ph,Me})Ni–S–2,4,6-$^i Pr_3C_6H_2$]. To a solid sample of NaS–2,4,6-$^i Pr_3C_6H_2$ (23 mg, 0.087 mmol) was added [(Tp^{Ph,Me})Ni–Cl] (50 mg, 0.086 mmol) dissolved in dichloromethane (10 mL) under argon. The solution changed color almost instantly to dark bluish-purple. After stirring 30 min, the solution was filtered through Celite and evaporated to dryness. The solids were redissolved in dichloromethane and layered with hexane. Slow diffusion at –38 °C gave purple crystals, which were recovered by filtration (51 mg, 0.065

mmol, 75% yield). Anal. calcd for $C_{45}H_{51}BN_6NiS$: C, 69.52; H, 6.61; N, 10.81. Found: C, 70.01; H, 6.69; N, 10.65. UV–vis–NIR (CH_2Cl_2): λ_{max} (ε) 345 (1.2); 445 (0.8); 549 (3.2); 738 (0.3); 922 nm (0.2 mM^{-1} cm^{-1}). ^1H NMR ($CDCl_3$, 295 K): δ 67.3 (3H, 4-pz); 30.3 (4H, *m*-SAr + *o,o*-^{i}Pr$_2$); 18.2 (1H, *p*-^{i}Pr); 10.6 (12H, *o,o*-^{i}Pr$_2$); 9.8 (6H, 3-*o*-Ph); 7.5 (6H, 3-*m*-Ph); 7.3 (3H, 3-*p*-Ph); 2.9 (9H, 5-Me); 2.4 (6H, *p*-^{i}Pr); –11.2 (1H, BH). μ_{eff} = 3.0 μ_B. FTIR (KBr): 2538 cm^{-1}, ν(B–H).

2.2. Synthesis of [(Tp^{Ph,Me})Ni(NCMe)(S–2,4,6-^{i}Pr$_3$C$_6$H$_2$)]. A second sample of [(Tp^{Ph,Me})Ni–S–2,4,6-^{i}Pr$_3$C$_6$H$_2$] was prepared in CH_2Cl_2 as described above. The solvent was removed under vacuum, and the purple solids were extracted into toluene and filtered. The filtrate was taken to dryness under vacuum, and the residue was extracted into a minimal volume (< 1 mL) of CH_3CN. The red solution was cooled to *ca*. -35 °C, and a mixture of red and purple crystals formed on standing several days. The mother liquor was decanted and the crystals were carefully washed with cold hexane. Red crystals of the CH_3CN adduct were recovered manually. FTIR (KBr): 2545, 2461 cm^{-1}, ν(B–H).

2.3. Synthesis and characterization of [(Tp^{Ph,Me})Ni–S–C$_6$H$_4$-4-OMe]. A sample of [(Tp^{Ph,Me})Ni–Cl] (30 mg, 0.052 mmol) was dissolved in toluene (15 mL) in a 50mL Schlenk flask under argon. To the solution was added NaS–C_6H_4-4-OMe (9 mg, 0.056 mmol). The solution changed color to dark brownish-blue. After stirring 4 h, the solution was filtered through Celite, and dried under vacuum. The solids were extracted into dichloromethane and layered with hexane. Slow diffusion produced violet crystals that were isolated by filtration (33 mg, 0.042 mmol, 81% yield). Anal. calcd for $C_{37}H_{35}BN_6NiOS{\bullet}H_2O$: C, 63.55; H, 5.33; N, 12.02; S, 4.59. Found: C, 63.13; H, 5.49; N, 11.79; S, 4.29. UV–vis–NIR (CH_2Cl_2): λ_{max} (ε) 346 (sh, 1.3); 383 (sh, 1.0); 540 (1.4); 715 (sh, 0.1); 910 nm (0.1 mM^{-1} cm^{-1}). ^1H NMR (CD_2Cl_2,

295 K): δ 71.1 (3H, 4-pz); 24.7 (2H, *m*-SAr); 10.2 (6H, 3-*o*-Ph); 8.1 (3H, *p*-OMe); 7.8 (6H, 3-*m*-Ph); 7.5 (3H, 3-*p*-Ph); 4.8 (9H, 5-Me); –10.4 (1H, BH) –31.5 (2H, *o*-SAr). FTIR (KBr): 2544 cm^{-1}, ν(B–H).

2.4. Synthesis and characterization of [(Tp^{Ph,Me})Ni–S–C$_6$H$_4$-4-Me]•½C$_6$H$_{14}$. The complex was synthesized as for the 4-OMe analogue above and obtained as violet crystals (32 mg, 0.045 mmol, 86% yield). Anal. Calcd for $C_{40}H_{42}BN_6NiS$: C, 67.82; H, 5.98; N, 11.86. Found: C, 68.53; H, 6.04; N, 12.17. UV–vis–NIR (CH_2Cl_2): λ_{max} (ε) 348 (sh, 1.4); 378 (sh, 1.0); 548 (1.7); 716 (sh, 0.2); 912 nm (0.1 mM^{-1} cm^{-1}). ^{1}H NMR (CD_2Cl_2, 295 K): δ 71.4 (3H, 4-pz); 49.4 (3H, *p*-SAr); 25.7 (2H, *m*-SAr); 10.1 (6H, 3-*o*-Ph); 7.8 (6H, 3-*m*-Ph); 7.5 (3H, 3-*p*-Ph); 4.8 (9H, 5-Me); –10.6 (1H, BH) –29.3 (2H, *o*-SAr). FTIR (KBr): 2543 cm^{-1}, ν(B–H).

2.5. Synthesis and characterization of [(Tp^{Ph,Me})Ni–S–C$_6$H$_4$-4-Cl]. The complex was synthesized as for the 4-OMe analogue above and obtained as dark red crystals (30 mg, 0.044 mmol, 85% yield). Anal. Calcd for $C_{36}H_{32}BClN_6NiS$: C, 63.06; H, 4.70; N, 12.26. Found: C, 63.04; H, 4.97; N, 12.00. UV–vis–NIR (CH_2Cl_2): λ_{max} (ε) 373 (1.1); 384 (sh, 1.0); 487 (sh, 1.1); 539 (1.8); 700 (sh, 0.2); 893 nm (0.1 mM^{-1} cm^{-1}). ^{1}H NMR (CD_2Cl_2, 295 K): δ 73.2 (3H, 4-pz); 25.8 (2H, *m*-SAr); 10.0 (6H, 3-*o*-Ph); 8.0 (6H, 3-*m*-Ph); 7.5 (3H, 3-*p*-Ph); 5.4 (9H, 5-Me); –10.6 (1H, BH) –28.0 (2H, *o*-SAr). FTIR (KBr): 2535 cm^{-1}, ν(B–H).

2.6 X-ray crystallography. Crystals of [(Tp^{Ph,Me})Ni–SPh], [(Tp^{Ph,Me})Ni–S–2,4,6-^{i}Pr$_3$C$_6$H$_2$]•CH_2Cl_2 and [(Tp^{Ph,Me})Ni(NCMe)(S–2,4,6-^{i}Pr$_3$C$_6$H$_2$)]•CH_3CN were placed on the tips of 0.1 mm diameter glass capillaries and mounted on a Bruker AXS diffractometer equipped with a CCD area detector and a nitrogen cryostat for low-temperature data collection.[24] The data collections were carried out using Mo Kα radiation (λ = 0.71073 Å, graphite monochromator). The intensity data were corrected for absorption and decay (SADABS).[25] Final cell constants

were calculated from strong reflections from the actual data collections after integration (SAINT).[26] The structures were solved by direct methods and difference Fourier analysis using SIR92[27] or SHELXS,[28] and refined using Bruker SHELXTL.[28] All non-hydrogen atoms were refined with anisotropic displacement parameters. All hydrogen atoms were placed in ideal positions and refined as riding atoms with relative isotropic displacement parameters. Thermal ellipsoid plots were drawn with Mercury.[29] Crystal and refinement data are summarized in Table 1. Relevant bond lengths and angles are listed in the figure captions and compared in Table 2.

The initial structure solution and refinement of [(Tp^{Ph,Me})Ni–S–2,4,6-^{i}Pr$_3$C$_6$H$_2$]•CH$_2$Cl$_2$ yielded an R1 value of *ca.* 7%. Inspection of the most disagreeable reflections suggested the presence of a minor non-merohedral twin. The program Cell_Now[30] did index a minor twin and the data was reintegrated as such. The data were re-corrected for absorption and scaling effects with TWINABS,[31] which improved the refinement by *ca.* 2%. The SHELXL twin matrix was

-0.998	-0.003	-0.640
0.001	-1.000	-0.001
-0.005	0.000	0.998

and the twin scale factor was 0.15861. The refinement was further improved by additional disorder modeling of the dichloromethane solvent.

2.7 DFT calculations. The experimental core structure of [(Tp^{Ph,Me})Ni(NCMe)(S–2,4,6-^{i}Pr$_3$C$_6$H$_2$)] was used to construct an initial model after replacement of pyrazole and arylthiolate substituents with hydrogen. Spin-unrestricted geometry optimization of a simplified [(Tp)Ni(NCMe)(SPh)] model under C_1 point symmetry was performed starting with the Amsterdam Density Functional software package (version 2008.01),[32,33] using the Vosko–Wilk–Nusair LDA local exchange-correlation functional,[34] the Becke–Perdew GGA corrections,[35,36]

and the TZDP basis set available in the ADF library with default convergence parameters and frozen atomic cores. Allowed excitations were calculated by TD-DFT methods.[37]

3.0. Results and Discussion

3.1 Synthesis of new thiolate complexes. Four new pseudotetrahedral nickel(II) arylthiolate complexes [($Tp^{Ph,Me}$)Ni–SAr] are reported herein (Ar = 2,4,6-$^{i}Pr_3C_6H_2$, 4-C_6H_4–Cl, 4-C_6H_4–Me, 4-C_6H_4–OMe). Together with previously reported complexes (Ar = Ph, 2,6-$Me_2C_6H_3$, 2,4,6-$Me_3C_6H_2$)[15] two series of complexes are encompassed, one with steric and electronic modifications arising from *ortho*- and *para*-substituted arylthiolates [($Tp^{Ph,Me}$)Ni–S–2,4,6-R"$_3C_6H_2$] (R" = H, Me, ^{i}Pr) and the other with electronic modification arising from *para* substitution [($Tp^{Ph,Me}$)Ni–S–C_6H_4-4-Y] (Y = Cl, H, Me, OMe). Comparison with previously reported [($Tp^{Me,Me}$)Ni–SAr] analogues also reveal steric effects arising from the proximal 3-pyrazole substituents.

Metatheses of [($Tp^{Ph,Me}$)Ni–Cl] with NaSAr were carried out in dry, non-coordinating solvents under argon, as previously described.[15,16] Successful metathesis was indicated by precipitation of NaCl and the appearance of an intense purple or blue color arising from ArS → Ni LMCT transitions. All new complexes were isolated as crystalline solids and characterized by elemental analysis, spectroscopy, and X-ray crystallography, as discussed in more detail below. The complexes dissolve intact into a wide range of low-polarity organic solvents (*e.g.*, toluene, THF, CH_2Cl_2), and readily react with O_2, H_2O and organic electrophiles in such solutions; a detailed investigation of this reactivity is reported separately.[17]

3.2 Introductory remarks on structure and bonding in [(Tp)Ni–SAr]. General features of the electronic structure for a C_{3v}-symmetric scorpionate complex [(Tp)Ni–X] (*e.g.*, X = halide) were discussed previously.[38] The metal d orbitals are split by the applied ligand field (*i.e.*, a_1 + 2 e): one degenerate pair of non-bonding orbitals (d_{xy}, $d_{x^2-y^2}$) and the Ni–X antibonding a_1 orbital (d_{z^2}) are filled and stabilized; the other degenerate pair (d_{xz}, d_{yz}) exhibit σ* character with respect to the tripodal nitrogen array, π* with respect to the apical X ligand, and are thus destabilized and singly occupied. This ligand field splitting yields a $^3A_2$ ground state for a d^8 Ni(II) ion.

Bending of the Ni–X bond vector off the three-fold axis stabilizes the filled Ni dσ – X pσ* interaction by mixing with one SOMO, leaving the other to support a X pπ – Ni dπ* interaction.[39] Depending on the directionality, ideally towards or away from a single pyrazole arm, this bending gives rise to limiting trigonal pyramidal and sawhorse configurations, respectively.[16] The degree of distortion can be quantified by the τ^4 parameter (τ^4 = [360° – α – β]/141°, where α and β are the two largest coordinate angles, τ^4 = 0.0 → 1.0 for $D_{4h} \rightarrow T_d$).[40] Within the scorpionate ligand, N–Ni–N angles are constrained to *ca.* 92(1)°; therefore, pseudotetrahedral complexes exhibit initial umbrella distortion with angles of 124(1)° between Ni–N bond vectors and an ideal 3-fold axis (*i.e.*, H–B•••Ni). This constraint sets an upper limit $t^4 \leq 0.81$ even for a C_{3v}-symmetric complex. Maximum off-axis bending to C_s-symmetric sawhorse or trigonal pyramidal conformations including one constrained N–Ni–N angle sets a lower limit $\tau^4 \geq 0.64$. Trigonal pyramidal bending is also quantified by an alternative τ parameter (Table 2), ranging from 0.0 (T_d) to 1.0 (ideal trigonal pyramid).[41]

A further complication arises upon substitution of an apical arylthiolate ligand. The S–C_{ipso} bonding interaction significantly stabilizes the co-linear sulfur p orbital, leaving one of the perpendicular p orbitals to support the pseudo-σ interaction in the bent geometry, while the other

retains π symmetry.[12] Therefore, arylthiolates typically coordinate with a nearly square Ni–S–Ar angle. This places the arylthiolate substituent in close proximity to the 3-pyrazole substituents, inducing steric effects on the coordination geometry.[15,16]

We previously reported the X-ray crystal structure of [($Tp^{Me,Me}$)Ni–SPh], which exhibited significant off-axis bending, τ^4 = 0.73 (Table 2).[15,16] A preferred trigonal pyramidal geometry was evident, with the sulfur bent primarily towards one pyrazole ring with the substituent disposed between the two other pyrazole rings and nearly coplanar with Ni–S bond. This conformation is thus identified by one small and two large N–Ni–S angles, with respect to the umbrella angle, as well as a modest Ni–S–C_{ipso}–C_{ortho} torsion. In contrast, the bulkier arylthiolate substituent in the structure of [($Tp^{Me,Me}$)Ni–S–2,6-$Ph_2C_6H_3$] forced adoption of the alternate sawhorse conformation, with the sulfur bent between two pyrazole rings and the substituent rotated over the third pyrazole, τ^4 = 0.74.[16] This geometry is identified by one large and two small N–Ni–S angles, as well as a large Ni–S–C_{ipso}–C_{ortho} torsion. In the context of the present work, a particular motivation was to determine the structural effects resulting from *ortho*-arylthiolate substitution in [($Tp^{Ph,Me}$)Ni–SAr] analogues, in which the presence of larger 3-pyrazole phenyl substituents would seem to preclude adoption of a comparable sawhorse conformation.

3.3. X-ray crystallography of [($Tp^{Ph,Me}$)Ni–S–2,4,6-$R''_3C_6H_2$] (R'' = H, ^iPr). X-ray crystal structures of [($Tp^{Ph,Me}$)Ni–SPh] and [($Tp^{Ph,Me}$)Ni–S–2,4,6-$^iPr_3C_6H_2$] were determined herein, and the structure of [($Tp^{Ph,Me}$)Ni–S–2,6-$Me_2C_6H_3$] was reported previously.[15] Additional structural data were not pursued; the overall geometry of [($Tp^{Ph,Me}$)Ni–S–C_6H_4-Y] (Y = Cl, Me, OMe) is expected to correspond closely to that of [($Tp^{Ph,Me}$)Ni–SPh], with only minor

modulation of the Ni–SAr bond length and conformational bending, while the structure of [($Tp^{Ph,Me}$)Ni–S–2,4,6-$Me_3C_6H_2$] would approximate that of the 2,6-xylyl analogue.

The crystal lattice of [($Tp^{Ph,Me}$)Ni–SPh] contains two independent molecules, which are essentially identical (Fig. 1 and Fig. S1, ESI†). Both structures are quite similar to that of [($Tp^{Me,Me}$)Ni–SPh],[15,16] with equivalent Ni–SPh bond lengths (Table 2). The average Ni–N bond length of 2.01(1) Å also compares well to the values of 1.986(7) Å for [($Tp^{Me,Me}$)Ni–SPh][15] and 1.99(1) Å for [($Tp^{Ph,Me}$)Ni–Cl].[23] The τ^4 values are also comparable, although the distribution of N–Ni–SAr bond angles about the umbrella angle show that the off-axis bending is more obviously trigonal in [($Tp^{Ph,Me}$)Ni–SPh]. One minor difference is the Ni–S–C_{ipso}–C_{ortho} torsion; the phenylthiolate ring is disposed parallel to the flanking 3-pyrazole phenyl substituents in [($Tp^{Ph,Me}$)Ni–SPh], while the ring is slighted canted over a smaller methyl substituent in [($Tp^{Me,Me}$)Ni–SPh] (Fig. S2, ESI†).[15,16] The structure of [($Tp^{Ph,Me}$)Ni–S–2,6-$Me_2C_6H_3$] was previously determined to reveal structural effects arising from the steric and electronic effects of *ortho* methyl substituents.[15] Compared with [($Tp^{Ph,Me}$)Ni–SPh], this complex exhibits enhanced trigonal bending (τ^4 = 0.67) and a significantly increased Ni–S–Ar angle of 116.51(7)°, which opens space for the inner methyl substituent within the pocket formed by adjacent pyrazole arms. The larger *ortho* substituents of [($Tp^{Ph,Me}$)Ni–S–2,4,6-$^{i}Pr_3C_6H_2$] force even greater trigonal (τ^4 = 0.66) and Ni–S–Ar bending, 119.9(1)°. Furthermore, the arylthiolate substituent is rotated about the Ni–S bond towards one of the 3-pyrazole phenyl substituents and canted heavily over it; the N_{ax}–Ni–S–C_{ipso} and average Ni–S–C_{ipso}–C_{ortho} torsions are 156° and 53°, respectively compared with average values of 176° and 5° in [($Tp^{Me,Me}$)Ni–SPh],[15] respectively. This disposition of the arylthiolate ring allows the inner isopropyl substituent to drop into the vacated space between the equatorial pyrazoles. A short axial Ni•••H—C "anagostic" contact is observed to the inner *ortho*

alkyl substituents for both [($Tp^{Ph,Me}$)Ni–S–2,6-$Me_2C_6H_3$] and [($Tp^{Ph,Me}$)Ni–S–2,4,6-$^{i}Pr_3C_6H_2$], at distances of 2.56 Å and 2.58 Å, respectively.[42]

Only modest differences are observed in the Ni–SAr bond lengths of these three [($Tp^{Ph,Me}$)Ni–SAr] structures, possibly reflecting competition between steric and electronic effects, as the bulkier arylthiolate ligands are also more basic.[43,44] The Ni–N bond lengths monotonically increase with the size of the *ortho* substituents, and are generally longer than those of [($Tp^{Me,Me}$)Ni–SAr] analogues, but the observed differences fall short of statistical significance. A general conjecture arising from these structural data would suggest that compared with [($Tp^{Me,Me}$)Ni–SAr] analogues,[16] the 3-pyrazole phenyl substituents in [($Tp^{Ph,Me}$)Ni–SAr] obviate the sawhorse conformation observed for [($Tp^{Me,Me}$)Ni–S–2,6-$Ph_2C_6H_3$],[16] such that larger and more basic *ortho*-disubstituted thiolates are forced to adopt an increasingly strained disposition with an enhanced trigonal distortion, while possibly compromising ligation of the supporting scorpionate tripod.

3.4 ^{1}H NMR Spectroscopic characterization of [($Tp^{Ph,Me}$)Ni–SAr]. ^{1}H NMR spectra of the arylthiolate complexes are consistent with complex formulations in all cases (Fig. 2 and 3, and Fig. S3–S9, ESI†). Notwithstanding the limiting C_s symmetry implied by the solid state structure of [($Tp^{Ph,Me}$)Ni–SPh], all three pyrazole rings are equivalent, as are both halves of the arylthiolate substituent, thus indicating rapid site exchange in solution. The magnetic susceptibility of two arylthiolate complexes were determined in solution by the Evans NMR method,[21] and observed μ_{eff} values (*i.e.*, 2.8–3.0 μ_B) are consistent with a $^{3}A_2$ (S = 1) ground state.[38]

Resonances in the various ^{1}H NMR spectra exhibited hyperfine shifts consistent with a contact shift mechanism.[5,13,15,47,48] For example, the thiolate ring resonances of [($Tp^{Ph,Me}$)Ni–

SPh] exhibit an upfield, downfield, and upfield shift pattern for the respective *ortho*, *meta* and *para* protons, indicative of π-polarization.[5,13,15,48] Consistent with this assignment,[5] the added methyl substituent resonances of [(Tp^{Ph,Me})Ni–S–2,6-$Me_2C_6H_3$] and [(Tp^{Ph,Me})Ni–S–2,4,6-$Me_3C_6H_2$] are shifted well downfield, and the isopropyl resonances of [(Tp^{Ph,Me})Ni–S–2,4,6-$Me_3C_6H_2$] also exhibit a similar shift pattern. Suggestive of competing spin delocalization, chemical shifts of the arylthiolate *meta* protons are nearly constant in the series [(Tp^{Ph,Me})Ni–S–2,4,6-R"$_3C_6H_2$] (R" = H, Me, ^{i}Pr), despite the increased solid-state Ni–S–C_{ipso}–C_{ortho} torsion. The *ortho* resonance of [(Tp^{Ph,Me})Ni–SPh] is also slightly downfield from the *para* resonance, while the *ortho* methyl resonance of [(Tp^{Ph,Me})Ni–S–2,4,6-$Me_3C_6H_2$] is well downfield at 92 ppm compared with the *para* methyl resonance at 57 ppm. A minor dipolar contribution is not excluded,[47] although the electronic ground state is an orbital singlet.[38]

A consistent pattern is observed for protons on the supporting scorpionate ligand.[15] For all complexes, the pyrazole 4-H ring proton is shifted downfield to *ca.* 70 ppm, the 5-methyl and *ortho* 3-phenyl resonances are shifted slightly downfield, while the *meta* and *para* 3-phenyl resonances fall close to limiting diamagnetic shifts, and the borohydride is shifted upfield to *ca.* –11 ppm. Reflecting particular proximity to the nickel(II) ion, protons on the *ortho* positions of arylthiolate and 3-phenyl pyrazole substituent rings are particularly broadened.[5,13] Compared with those of the [(Tp^{Me,Me})Ni–SPh] analogue,[15] the chemical shifts of the 4-pyrazole proton of [(Tp^{Ph,Me})Ni–SPh] are smaller in $CDCl_3$, 77 versus 71 ppm, while those on the arylthiolate ring protons are larger, –19 versus –28 and –27 versus –38 ppm for the *ortho* and *para* protons, respectively. This comparison implies a shift of spin density from the scorpionate ligand to the arylthiolate co-ligand in [(Tp^{Ph,Me})Ni–SPh]. This trend is extended for the bulkier electron-rich thiolate complexes; the 4-pyrazole proton shifts of [(Tp^{Ph,Me})Ni–S–2,4,6-R"$_3C_6H_2$] (R" = Me, ^{i}Pr)

are further reduced to 67 ppm, while the thiolate *para* proton of [(Tp^{Ph,Me})Ni–S–2,6-$Me_2C_6H_3$] resonates at –43 ppm (Fig. 2). Spectra of the *para*-substituted series [(Tp^{Ph,Me})Ni–S–C_6H_4–4-Y] (Y = Cl, Me, OMe) in CD_2Cl_2 are all very similar. The pyrazole 4-H shift decreases slightly from 73 to 71 ppm between Cl and OMe, with an offsetting increase in the arylthiolate *ortho* shift, from –28 to –32 ppm (Fig. 3). These trends support the prior suggestion that scorpionate ligation in [(Tp^{Ph,Me})Ni–SAr] is somewhat compromised by the 3-pyrazole phenyl substituents, as well as by increasingly bulky and/or electron-rich thiolates.

3.5 UV-Vis-NIR spectroscopic characterization of [(Tp^{Ph,Me})Ni–SAr]. Electronic spectra of [(Tp^{Ph,Me})Ni–SAr] in CH_2Cl_2 solutions display several diagnostic features akin to those previously assigned for [(Tp^{Me,Me})Ni–SAr] and related pseudotetrahedral arylthiolate complexes (Fig. 4 and 5).[12–16] These include near-IR ligand field bands, visible ArS–Ni LMCT bands, as well as metal–ligand CT and intraligand bands in the UV region. However, the ligand field and LMCT bands of [(Tp^{Ph,Me})Ni–SAr] are somewhat red-shifted compared with [(Tp^{Me,Me})Ni–SAr] analogues, resulting in a complex color from red in the latter to purple or blue in the former.[15,16] This effect would be consistent with generally weaker scorpionate ligation that stabilizes the nickel dσ* acceptor orbitals.[16] The visible ArS–N LMCT bands also show a significant increase in extinction with increasing arylthiolate ring substitution within the series [(Tp^{Ph,Me})Ni–S–2,4,6-R"$_3C_6H_2$] (R" = H, Me, ^{i}Pr; Fig. 4). This may reflect both increased S pπ – Ni dπ* overlap resulting from enhanced trigonal bending,[13] as well as sterically-enforced rotation of the arylthiolate substituent that enhances S p contribution to the relevant molecular orbitals by decreasing overlap with the increasingly orthogonal aromatic ring.[14] Such arguments imply that the solid-state configurations are retained in solution. In contrast, no significant trends in the transition energies could be elucidated, which is also true of the *para*-substituted series

[($Tp^{Ph,Me}$)Ni–S–C_6H_4-4-Y] (Y = Cl, H, Me, OMe). This latter series of complexes may exhibit weak red-shifting of the ArS–Ni LMCT features with increasing thiolate basicity (Fig. 5),[42,43] as reported for [($Tp^{Me,Me}$)Ni–S–C_6H_4-4-Y] analogues,[16] but with decreased extinction. The similarity of spectra within this series is consistent with retention of the core structure elucidated for [($Tp^{Ph,Me}$)Ni–SPh]; in particular, the relatively low LMCT extinction may reflect the lack of Ni–S–C_{ipso}–C_{ortho} torsion.

3.6 FTIR spectroscopic characterization of [($Tp^{Ph,Me}$)Ni–SAr]. Compared with the rich electronic and NMR spectra, the FTIR data were relatively uninformative. Spectra of the four new arylthiolate complexes are shown (Fig. S10–S17, ESI†). While the spectra are broadly consistent with the assigned structures, arylthiolate modes are largely occluded by similar modes arising from scorpionate ligand substituents. Observation of ν(B–H) modes above 2500 cm^{-1} is consistent with κ^3-scorpionate ligation in all cases.[48]

3.7 Solvent binding to [($Tp^{Ph,Me}$)Ni–S–2,4,6-$^{i}Pr_3C_6H_2$]. Electronic spectra of [($Tp^{R,Me}$)Ni–SAr] typically do not vary significantly in aprotic organic solvents over a wide range of polarity (*i.e.*, toluene, CH_2Cl_2, CH_3CN).[15] This has been demonstrated specifically for [($Tp^{Ph,Me}$)Ni–S–2,4,6-$Me_3C_6H_2$] (Fig. S18, ESI†) and for [($Tp^{Me,Me}$)Ni–SPh].[18] In contrast, [($Tp^{Ph,Me}$)Ni–S–2,4,6-$^{i}Pr_3C_6H_2$] exhibits anomalous behavior, with the typical purple color in non-coordinating CH_2Cl_2 turning distinctly red in CH_3CN. Comparison of the electronic spectra recorded in the two solvents at room temperature (295 K) show the NIR ligand field bands and the ArS–Ni LMCT feature (at 550 nm in CH_2Cl_2) of the pseudotetrahedral complex are significantly diminished in CH_3CN, and an intense new feature appears at 396 nm (Fig. 6). These changes are attributed to formation of a CH_3CN adduct. Cooling the CH_3CN solution prompted further growth of the 396 nm feature at the expense of the pseudotetrahedral charge

transfer band, with an intervening isosbestic point at 456 nm (Fig. S19, ESI†). Curiously, this was not fully reversible; re-heating of the solution beyond room temperature resulted in selective bleaching of the 396 nm feature, consistent with arylthiolate ionization.

To obtain a solid sample of the adduct, a concentrated CH_3CN solution was cooled to *ca.* 238 K, and a mixture of purple and red crystals was obtained on standing. An FTIR spectrum of the crystals showed two ν(B–H) modes, at 2545 and 2460 cm^{-1} (Fig. S20, ESI†); the latter is clearly indicative of κ^2-scorpionate ligation.[49] Given the steric contacts evident in the crystal structure of the pseudotetrahedral complex, we assumed that one arm of the scorpionate is displaced by a single solvent molecule, yielding square planar [(κ^2-$Tp^{Ph,Me}$)Ni(NCMe)(SAr)]. This behavior contrasts with the electron-poor complex [($Tp^{Me,Me}$)Ni–SC_6H_4-4-NO_2] that yields an octahedral bis(acetontrile) adduct [(κ^3-$Tp^{Me,Me}$)Ni(NCMe)$_2$(SAr)] in CH_3CN.[18]

The square-planar structure was confirmed by low-temperature X-ray crystallography following judicious selection of a red single crystal (Fig. 7). A bidentate scorpionate ligand was indeed found, with one pyrazole arm detached from and rotated away from nickel, with a Ni•••B–N–N torsion angle of 116.0(1)°. The coordination geometry of the N_3S ligand field was nearly square planar (τ^4 = 0.09); the coordinate bond angles about nickel averaged 90° ± 2° (*cis*) and 175° ± 2° (*trans*), and the nickel atom was separated by 0.033 Å from an N_3S least-squares plane fitted to the four donor atoms. Compared with the average Ni–N bond length of 2.038(6) Å in the pseudotetrahedral complex, the Ni–N bond lengths were much shorter in the adduct: 1.934(1) Å for the pyrazole disposed *trans* to the thiolate; 1.886(1) Å for the pyrazole *trans* to the added acetonitrile; and 1.850(2) Å for the acetonitrile ligand itself, which was otherwise unremarkable. The Ni–S bond length of 2.1954(5) Å and Ni–S–Ar angle of 111.22(6)° are only

slightly diminished from those of the pseudotetrahedral complex, 2.210(1) Å and 119.9(1)°, respectively.

The bonding and electronic spectroscopy of the square-planar adduct was further elucidated by single-point DFT and TD-DFT calculations on a simplified [(κ^2-Tp)Ni(NCMe)(SPh)] model, obtained by optimization of the core structure for [($Tp^{Ph,Me}$)Ni(NCMe)(S–2,4,6-$^i Pr_3C_6H_2$)] determined by X-ray crystallography, following replacement of the arylthiolate and pyrazole substituents with hydrogen. Final coordinates for the optimized model are tabulated (Table S1, ESI†), and compared to the experimental structure (Fig. S21, ESI†). Isocontour plots of frontier orbitals are also shown in (Fig. S22, ESI†). Allowed excitations were calculated by TD-DFT methods (Table S2, ESI†).[37] Removal of the 3-pyrazole and *ortho* arylthiolate substituents eliminated a short interligand contact, which enabled a slight flexing of the equatorial ligand plane upon optimization of the model. The adduct model was stabilized in the gas-phase calculations by 0.06 eV (1.4 kcal/mol) relative to the sum of [(κ^3-Tp)Ni–SPh] and free CH_3CN; the equilibrium position implied by the solvent-dependent UV-Vis–NIR data is consistent with $\Delta G° = 0.2$ kcal/mole at 295 K for the experimental complexes in CH_3CN. Calculations on pseudotetrahedral [(κ^3-Tp)Ni–SPh] and related complexes were reported previously.[12,14,16]

Although interpretation of the calculated electronic structure is complicated by the lack of symmetry and the disparate bonding within the ligand set, the results were generally similar to previous calculations on nickel(II) complexes with square-planar N_3S ligand fields.[50,51] As expected for a diamagnetic d^8 metal ion, the LUMO is predominantly a dσ* orbital (71a, 46% d_{x2-y2}), destabilized by 1.3 eV relative to the HOMO, a highly covalent Ni–SAr π* interaction (70a; 46% S p_z, 40% Ni d_{yz}). Compared with these antibonding orbitals, the corresponding σ (S

p_y, 63a) and π (Ni d_{yz}, 64a) orbitals are stabilized by 2.6 and 1.1 eV, respectively. The axial lone pair (69a, d_{z^2}), lies only 0.3 eV below the HOMO. The two remaining d orbitals (66a, d_{xz} and 61a, d_{xy}) respectively fall 0.7 and 1.6 eV below the HOMO, the former being destabilized by π* interactions with a pyrazole ring and the *trans* acetonitrile ligand, and the latter remaining effectively non-bonding despite minor contributions from the ligands. Besides the nickel d and sulfur p atomic orbitals, additional filled frontier molecular orbitals are derived from the one-node Huckel π orbitals on the aromatic pyrazole (57a, 59a, 60a, 62a, 67a and 68a) and arylthiolate substituent rings (56a and 58a), as well as the lone pair on the detached nitrogen (67a). Besides the LUMO, four additional acceptor orbitals were found at 3.0-3.5 eV above the HOMO, comprised of acetonitrile π* orbitals (72a and 74a) and two-node Huckel π* orbitals on the arylthiolate substituent ring (73a and 75a). Just above these were the two-node π* orbitals on the pyrazole rings (76a, etc.).

The main differences in Ni–SAr bonding and spectroscopy between the pseudotetrahedral and square planar geometries arise principally from disproportionation of the nearly degenerate SOMOs in the former, to give a stabilized non-bonding lone pair (HOMO-1, 69a) and the LUMO (71a) with σ* symmetry in the latter (*i.e.*, d_{z^2} and $d_{x^2-y^2}$, respectively). As the SOMOs also exhibit Ni–N σ* character, this results in significantly shortened Ni–N bond lengths in the adduct. This same argument applies to the Ni–SAr bond, but the enhanced σ bonding is mitigated by unfavorable π* overlap in the adduct HOMO (70a), so only a modest decrease is obtained, both computationally and experimentally. Orthogonal Ni–S–C_{ipso}–C_{ortho} torsions switch the symmetries of the sulfur p donor orbitals (*i.e.*, from σ in the pseudotetrahedral complex to π in the square planar adduct for the orbital co-planar with the substituent, and vice-versa for the perpendicular orbital).

TD-DFT calculations were also performed on the optimized adduct model. The lowest 50 spin-allowed single-electron transitions were calculated, and compared to the electronic spectrum of the CH_3CN adduct, extrapolated from the normalized difference of spectra recorded in CH_2Cl_2 and CH_3CN (Fig. 6 and 8), assuming a simple equilibrium and the invariance of the pseudotetrahedral complex spectrum between the solvents. Notwithstanding simplification of the model, reasonable agreement between the extrapolated spectrum and calculated transition energies and intensities was obtained; moreover, the spectrum of the adduct is very similar to that reported for a square planar N_3S complex of nickel(II) with imidazole and alkylthiolate donors.[51] The alteration in bonding and frontier orbitals compared with the pseudotetrahedral precursor is obviously reflected in the electronic spectra. Most notably, a four-electron ArS pπ – Ni dπ* interaction is obtained in the square planar geometry, and the intense visible ArS–Ni LMCT bands of the pseudotetrahedral complex are completely extinguished. The intense UV feature of the adduct is revealed as a composite of three strong transitions between several ligand moieties and the metal-centered LUMO, as well as transitions from the covalent HOMO to π* acceptor orbitals localized on the acetonitrile ligand and the arylthiolate ring (*i.e.*, calculated transitions 13–15, Fig. 8 and Table S2, ESI†). The two electron ArS πs – Ni pσ* interaction supports weak LMCT absorption appearing as the visible tail (*e.g.*, transitions 7 and 9). Additional visible and NIR bands are assigned by the calculations as the ligand field (*i.e.*, transitions 1, 4, 5 and 6) and pyrazole LMCT transitions (*i.e.*, transitions 3, 8 and 10). Compared with the NIR bands of the pseudotetrahedral complex, these transitions are blue-shifted by destabilization of the adduct LUMO. More definitive assignments are precluded by the low symmetry and the plethora of relevant donor and acceptor orbitals (Fig. S22, ESI†).

4.0 Summary

We have reported several new pseudotetrahedral arylthiolate complexes [($Tp^{Ph,Me}$)Ni–SAr] with two specific patterns of *ortho* and/or *para* arylthiolate substitution intended to elicit steric (*i.e.*, [($Tp^{Ph,Me}$)Ni–S–2,4,6-R"$_3C_6H_2$]: R" = H, Me, ^{i}Pr) and/or electronic (*i.e.*, [($Tp^{Ph,Me}$)Ni–S–C_6H_4-4-Y]: Y = Cl, H, Me, OMe) effects on arylthiolate coordination. Unlike the [($Tp^{Me,Me}$)Ni–SAr] analogues, which equilibrate into a sawhorse conformation upon introduction of *ortho* arylthiolate substituents, [($Tp^{Ph,Me}$)Ni–SAr] analogues with a larger 3-pyrazole substituent exhibit enhanced trigonal bending, with evidence of increasing steric restriction in the disposition of bulkier substituents. Generally weaker scorpionate ligation is also implied by red-shifting of ligand field and ArS–Ni LMCT bands, as well as a relative shift of spin density onto the arylthiolate co-ligand, as evidenced by ^{1}H NMR contact shifts. More modest spectroscopic effects were noted in the series of [($Tp^{Ph,Me}$)Ni–S–C_6H_4-4-Y] complexes. The most electron-rich and sterically encumbered complex [($Tp^{Ph,Me}$)Ni–S–2,4,6-$^{i}Pr_3C_6H_2$] dissolves in neat CH_3CN to give a unique square planar solvent adduct with κ^2-scorpionate ligation. The electronic spectrum and bonding in the adduct were elucidated with the assistance of single-point DFT and TD-DFT calculations on a simplified [(κ^2-Tp)Ni(NCMe)(SPh)] model. Comparison with [(κ^3-Tp)Ni–SPh] highlights the intrinsic differences in Ni–SAr bonding and spectroscopy between square planar and pseudotetrahedral geometries.

Acknowledgments

The authors acknowledge the donors of the American Chemical Society Petroleum Research Fund (49296-DNI3) for support of this research. We also thank the Ohio University 1804 Fund for support in acquiring the DFT computational facility.

Table of Contents Entry

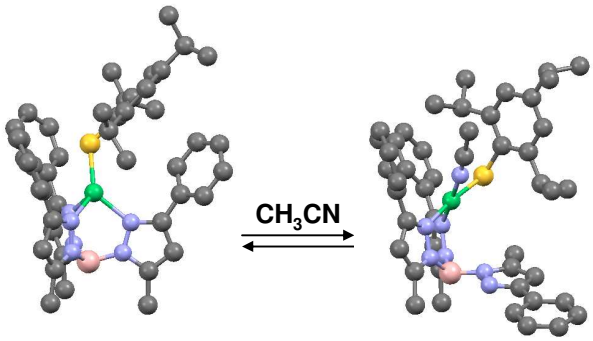

Substitution on arylthiolates in pseudotetrahedral nickel(II) complexes [($Tp^{Ph,Me}$)Ni–SAr] reveal steric and electronic effects on Ni–SAr bonding and spectroscopy, including pyrazole arm dechelation (pictured).

References

1. Y. Li and D. B. Zamble, *Chem. Rev*., 2009, **109**, 4617–4643.

2. E. I. Solomon, S. I. Gorelsky and A. Dey, *J. Comput. Chem*., 2006, **27**, 1415–1428.

3. C. A. Grapperhaus and M. Y. Darensbourg, *Acc. Chem. Res*., 1998, **31**, 451–459.

4. S. A. Ivanov, M. A. Kozee, W. A. Merrill, S. Agarwal and L. F. Dahl, *J. Chem. Soc, Dalton Trans*., 2002, 4105–4115.

5. D. Swenson, N. C. Baenziger and D. Coucouvanis, *J. Am. Chem. Soc*., 1978, **100**, 1932–1934.

6. S. G. Rosenfield, W. H. Armstrong and P. K. Mascharak, *Inorg. Chem*., 1986, **25**, 3014–3018.

7. A. Silver, S. A. Koch and M. Millar, *Inorg. Chim. Acta*., 1993, **205**, 9–14.

8. A. Mueller and G. Henkel, *Z. Naturforsch. B*, 1995, **50**, 1464–1468.

9. T. Nguyen, A. Panda, M. M. Olmstead, A. F. Richards, M. Stender, M. Brynda and P. P. Power, *J. Am. Chem. Soc*., 2005, **127**, 8545–8552.

10. C. E. MacBeth, J. C. Thomas, T. A. Betley and J. C. Peters, *Inorg. Chem.*, 2004, **43**, 4645–4662.

11. Y. Matsunaga, K. Fujisawa, N. Ibi, Y. Miyashita and K. Okamoto, *Inorg. Chem*., 2005, **44**, 325–335.

12. S. I. Gorelsky, L. Basumallick, J. Vura-Weis, R. Sarangi, K. O. Hodgson, B. Hedman, K. Fujisawa and E. I. Solomon, *Inorg. Chem*., 2005, **44**, 4947–4960.

13. J. Cho, G. P. A. Yap and C. G. Riordan, *Inorg. Chem*., 2007, **46**, 11308–11315.

14. K. M. Van Heuvelen, J. Cho, T. Dingee, C. G. Riordan and T. C. Brunold, *Inorg. Chem*., 2010, **49**, 6535–6544.

15. S. Chattopadhyay, T. Deb, H. Ma, J. L. Petersen, V. G. Young, Jr. and M. P. Jensen, *Inorg. Chem*., 2008, **47**, 3384–3392.

16. S. Chattopadhyay, T. Deb, J. L. Petersen, V. G. Young, Jr. and M. P. Jensen, *Inorg. Chem*., 2010, **49**, 457–467.

17. T. Deb and M. P. Jensen, *Inorg. Chem*., 2014, submitted.

18. J. Nakazawa, H. Ogiwara, Y. Kashiwazaki, A. Ishii, N. Imamura, Y. Samejima and S. Hikichi, *Inorg. Chem.*, 2011, **50**, 9933–9935.

19. S. Trofimenko, *Chem. Rev.*, 1993, **93**, 943–980.

20. MestReNova, version 5.1.0, Mestrelab Research, Santiago de Compostela, 2007.

21. D. F. Evans and D. A. Jakubovic, *J. Chem. Soc., Dalton Trans.*, 1988, 2927–2933.

22. A. L. Rheingold, R. L. Ostrander, B. S. Haggerty and S. Trofimenko, *Inorg. Chem.*, 1994, **33**, 3666–3676.

23. K. Uehara, S. Hikichi and M. Akita, *J. Chem. Soc., Dalton Trans.*, 2002, 3529–3538.

24. SMART, version 5.054, Bruker Analytical X-ray Systems, Madison, WI, 2001.

25. R. H. Blessing, *Acta Crystallogr.*, 1995, **A51**, 33–38.

26. SAINT+, version 6.45, Bruker Analytical X-Ray Systems, Madison, WI, 2003.

27. A. Altomare, G. Cascarano, C. Giacovazzo, A. Guagliardi, M. C. Burla, G. Polidori and M. Camalli, *J. Appl. Crystallogr.*, 1994, **27**, 435.

28. SHELXTL, version 6.14, Bruker Analytical X-Ray Systems, Madison, WI, 2000.

29. Mercury, version 3.3.1, Cambridge Crystallographic Data Centre, Cambridge, U.K., 2013.

30. G. M. Sheldrick, CELL_NOW, version 2, Bruker Analytical X-Ray Systems, Madison, WI, 2008.

31. G. M. Sheldrick, TWINABS, version 2, Bruker Analytical X-Ray Systems, Madison, WI, 2008.

32. ADF, version 2008.01, Scientific Computing and Modelling NV, Vrije Universiteit, Amsterdam, The Netherlands, 2008.

33. G. te Velde, F. M. Bickelhaupt, E. J. Baerends, C. Fonseca Guerra, S. J. A. van Gisbergen, J. G. Snijders and T. Ziegler, *J. Comput. Chem.*, 2001**, 22**, 931–967.

34. S. H. Vosko, L. Wilk and M. Nusair, *Can. J. Phys.*, 1980, **58**, 1200–1211.

35. A. D. Becke, *Phys. Rev. A*, 1988, **38**, 3098–3100.

36. J. P. Perdew, *Phys. Rev. B*, 1986, **33**, 8822–8824.

37. S. J. A. van Gisbergen, J. G. Snijders and E. J. Baerends, *Comput. Phys. Commun*., 1999, **118**, 119–138.

38. P. J. Desrochers, J. Telser, S. A. Zvyagin, A. Ozarowski, J. Krzystek and D. A. Vicic, *Inorg. Chem*., 2006, **45**, 8930–8941.

39. J. L. Detrich, R. Konečný, W. M. Vetter, D. Doren, A. L. Rheingold and K. H. Theopold, *J. Am. Chem. Soc*., 1996, **118**, 1703–1712.

40. L. Yang, D. R. Powell and R. P. Houser, *Dalton Trans*., 2007, 955–964.

41. J. Vela, S. Stoian, C. J. Flaschenriem, E. Münck and P. L. Holland, *J. Am. Chem. Soc*., 2004, **126**, 4522–4523.

42. M. Brookhart, M. L. H. Green and G. Parkin, *Proc. Natl Acad. Sci. U.S.A.*, 2007, **104**, 6908–6914.

43. P. De Maria, A. Fini and F. M. Hall, *J. Chem. Soc., Perkin Trans. 2*, 1973, 1969–1971.

44. P. De Maria, A. Fini and F. M. Hall, *J. Chem. Soc., Perkin Trans. 2*, 1974, 1443–1445.

45. G. R. Fulmer, A. J. M. Miller, N. H. Sherden, H. E. Gottlieb, A. Nudelman, B. M. Stoltz, J. E. Bercaw and K. I. Goldberg, *Organometallics*, 2010, **29**, 2176–2179.

46. T. Deb, G. T. Rohde, V. G. Young, Jr. and M. P. Jensen, *Inorg. Chem*., 2012, **51**, 7257–7270.

47. J. P. Jesson, *J. Chem. Phys*., 1967, **47**, 582–591.

48. M. S. Ram, C. G. Riordan, R. Ostrander and A. L. Rheingold, *Inorg. Chem.*, 1995, **34**, 5884–5892.

49. T. O. Northcutt, R. J. Lachicotte and W. D. Jones, *Organometallics*, 1998, **17**, 5148–5152.

50. C. S. Mullins, C. A. Grapperhaus, B. C. Frye, L. H. Wood, A. J. Hay, R. M. Buchanan and M. S. Mashuta, *Inorg. Chem*., 2009, **48**, 9974–9976.

51. R. M. Jenkins, M. L. Singleton, E. Almaraz, J. H. Reibenspies and M. Y. Darensbourg, *Inorg. Chem*., 2009, **48**, 7280–7293.

Table 1. Summary of X-ray Crystallography

Compound	[(Tp^{Ph,Me})Ni–SPh]	[(Tp^{Ph,Me})Ni–S–2,4,6-^{i}Pr$_3$C$_6$H$_2$]•CH$_2$Cl$_2$	[(Tp^{Ph,Me})Ni(NCMe)(S–2,4,6-^{i}Pr$_3$C$_6$H$_2$)]•CH$_3$CN
Empirical formula	$C_{36}H_{33}BN_6NiS$	$C_{46}H_{53}BCl_2N_6NiS$	$C_{49}H_{57}BN_8NiS$
Formula weight	651.26	862.42	859.61
Temperature (K)	123(2)	173(2)	123(2)
Crystal system	Monoclinic	Monoclinic	Triclinic
Space group	$P2_1/n$	$P2_1/c$	P-1
a (Å)	19.400(2)	18.656(6)	11.202(1)
b (Å)	11.137(1)	11.210(4)	11.843(1)
c (Å)	29.827(3)	22.998(8)	19.114(2)
α (deg)	90	90	98.018(1)
β (deg)	95.868(1)	113.227(5)	95.892(1)
γ (deg)	90	90	111.318(1)
V (Å^3)	6411(1)	4420(3)	2306.7(4)
Z	8	4	2
Density (calc, g/cm^3)	1.350	1.296	1.238
Absorption coefficient (mm^{-1})	0.706	0.647	0.508
Crystal color, morphology	Purple, plate	Purple, plate	Red, block
Crystal size (mm)	0.40 x 0.30 x 0.08	0.50 x 0.25 x 0.04	0.40 x 0.35 x 0.30
Reflections collected	75369	15589	27102
Independent reflections (R_{int})	13094 (0.0598)	7830 (0.0480)	9396 (0.0339)
Observed reflections	9792	6404	7750
Data/restraints/parameters	13094/0/817	7830/28/552	9396/0/552
GOF	1.019	1.041	1.038
*R*1, *wR*2 [$I > 2\sigma(I)$]	0.0395, 0.0839	0.0493, 0.1110	0.0333, 0.0772
*R*1, *wR*2 (all data)	0.0637, 0.0944	0.0681, 0.1208	0.0471, 0.0850
Difference peak, hole (e/ Å^3)	0.530, –0.521	0.591, –0.418	0.410, –0.253

Table 2. Geometric and conformational comparison of pseudotetrahedral arylthiolate complexes.

Complex	Ni–SAr (Å)	Ni–N, average (Å)	Ni–S–Ar, (deg)	N–Ni–N, average (deg)	N–Ni–SAr (deg)	Umbrella angle (deg)[a]	τ^4 [b]	τ[c]	Ni–SAr torsion, average (deg)	ref.
[($Tp^{Me,Me}$)Ni–S–2,6-$Ph_2C_6H_3$]	2.2589(6)	1.997(4)	100.11(7)	91.5(5)	140.01(6), 115.47(4), 115.47(4)	124.2	0.74		89.5	16
[($Tp^{Me,Me}$)Ni–S–C_6H_4-4-NO_2]	2.2438(9)	1.984(4)	101.59(7)	91.9(4)	130.95(5), 124.21(5), 115.77(5)	123.9	0.74	0.54	32.4	18
[($Tp^{Me,Me}$)Ni–SPh]	2.2162(8)	1.986(7)	103.84(8)	92(1)	134.69(6), 122.69(6), 113.26(6)	124.0	0.73	0.60	16.4	15
[($Tp^{Ph,Me}$)Ni–SPh][d]	2.2160(7)	2.01(1)	104.30(8)	91.5(2)	130.90(6), 126.50(6), 114.22(6)	124.2	0.73	0.57	2.7	(e)
	2.2224(7)	2.012(7)	106.63(8)	92(1)	131.42(6), 129.21(6), 109.85(6)	124.1	0.70	0.63	7.0	
[($Tp^{iPr,iPr}$)Ni–SC_6F_5][d]	2.259(2)	1.99(1)	106.2(2)	92(2)	132.7(1), 128.9(1), 106.8(1)	124.0	0.70	0.72	11.0	11
	2.259(1)	2.00(1)	105.4(1)	92(1)	132.8(1), 128.4(1), 106.40(8)	123.8	0.70	0.72	10.3	
[($Tp^{Ph,Me}$)Ni–S–2,6-$Me_2C_6H_3$]	2.1978(5)	2.027(7)	116.51(7)	90.7(8)	135.73(5), 129.95(5), 103.05(5)	124.8	0.67	0.81	15.2	15
[($Tp^{Ph,Me}$)Ni–2,4,6-$^i Pr_3C_6H_2$]	2.210(1)	2.038(6)	119.9(1)	91(4)	136.13(9), 130.53(9), 99.61(9)	124.3	0.66	0.83	53.0	(e)
[($PhTt^{tBu}$)Ni–SPh][f]	2.187(1)		111.6(1)			122.3	0.72	0.69	1.3	13
[($PhTt^{tBu}$)Ni–SC_6F_5][f]	2.2355(9)		110.48(7)			122.9	0.72	0.74	6.3	13
[($PhBP_3$)Ni–SC_6H_4-4-^{t}Bu][g]	2.1188(8)		106.70(9)			120.4	0.70		68.0	10

(a) average angle between Ni–N bond vectors and 3-fold Ni•••B axis. (b) $\tau^4 = (360° - \alpha - \beta)/141°$, where α and β are the two largest angles.[40] (c) $\tau = [\Sigma(\text{basal–Ni–basal}) - \Sigma(\text{apical–Ni–basal})]/90°$.[41] (d) crystallographically independent molecules. (e) this work. (f) $PhTt^{tBu}$ = phenyltris(*tert*-butylthiomethyl)borate, $PhB(CH_2S^tBu)_3$. (g) $PhBP_3$ = phenyltris(diphenylphosphinomethyl)borate, $PhB(CH_2PPh_2)_3$.

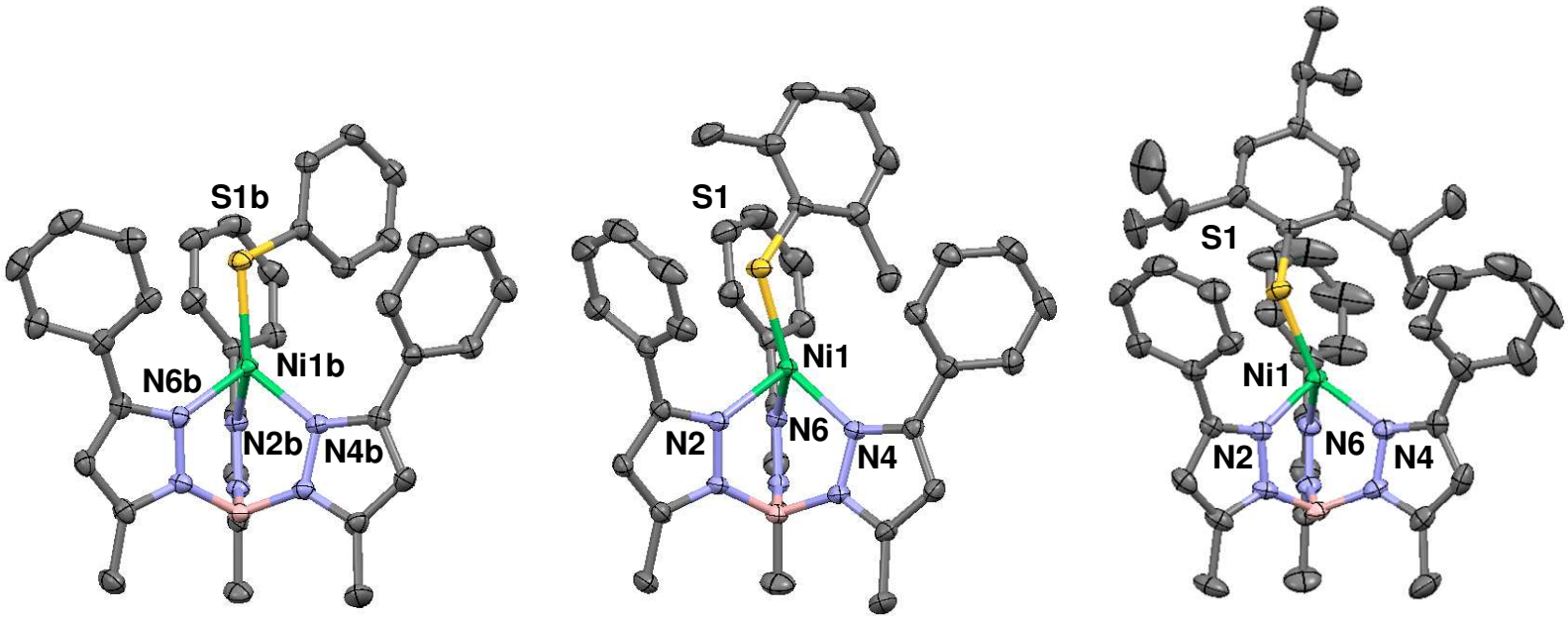

Fig. 1. Thermal ellipsoid plots (50% probability) of [(Tp^{Ph,Me})Ni–SPh] (left; independent molecule "a" shown in Fig. S1, ESI†), [(Tp^{Ph,Me})Ni–S–2,6-$Me_2C_6H_3$] (center),[15] and [(Tp^{Ph,Me})Ni–S–2,4,6-$^{i}Pr_3C_6H_2$] (right). Hydrogen atoms are omitted for clarity. Coordinate bond lengths for [(Tp^{Ph,Me})Ni–SPh] (Å): Ni1b–N2b, 2.018(2); Ni1b–N4b, 1.997(2); Ni1b–N6b, 2.019(2); Ni1b–S1b, 2.2160(7). Coordinate bond angles for [(Tp^{Ph,Me})Ni–SPh] (°): N2b–Ni1b–N4b, 91.29(8); N2b–Ni1b–N6b, 91.76(8); N4b–Ni1b–N6b, 91.45(8); N2b–Ni1b–S1b, 130.90(6); N4b–Ni1b–S1b, 126.50(6); N6b–Ni1b–S1b, 114.22(6); Ni1b–S1b–C31b, 104.30(8). Coordinate bond lengths for [(Tp^{Ph,Me})Ni–S–2,6-$Me_2C_6H_3$] (Å): Ni1–N2, 2.032(2); Ni1–Ni4, 2.019(2); Ni1–N6, 2.030(2); Ni1–S1, 2.1978(5). Coordinate bond angles for [(Tp^{Ph,Me})Ni–S–2,6-$Me_2C_6H_3$] (°): N2–Ni1–N4, 89.70(6); N2–Ni1–N6, 91.02(6); N4–Ni1–N6, 91.23(6); N2–Ni1–S1, 103.05(5); N4–Ni1–S1, 135.73(5); N6–Ni1–S1, 129.95(5); Ni1–S1–C31, 116.51(7). Coordinate bond lengths for [(Tp^{Ph,Me})Ni–S–2,4,6-$^{i}Pr_3C_6H_2$] (Å): Ni1–N2, 2.038(3); Ni1–Ni4, 2.032(3); Ni1–N6, 2.043(3); Ni1–S1, 2.210(1). Coordinate bond angles for [(Tp^{Ph,Me})Ni–S–2,4,6-$^{i}Pr_3C_6H_2$] (°): N2–Ni1–N4, 88.0(1); N2–Ni1–N6, 95.1(1); N4–Ni1–N6, 91.1(1); N2–Ni1–S1, 99.61(9); N4–Ni1–S1, 136.13(9); N6–Ni1–S1, 130.53(9); Ni1–S1–C31, 119.9(1).

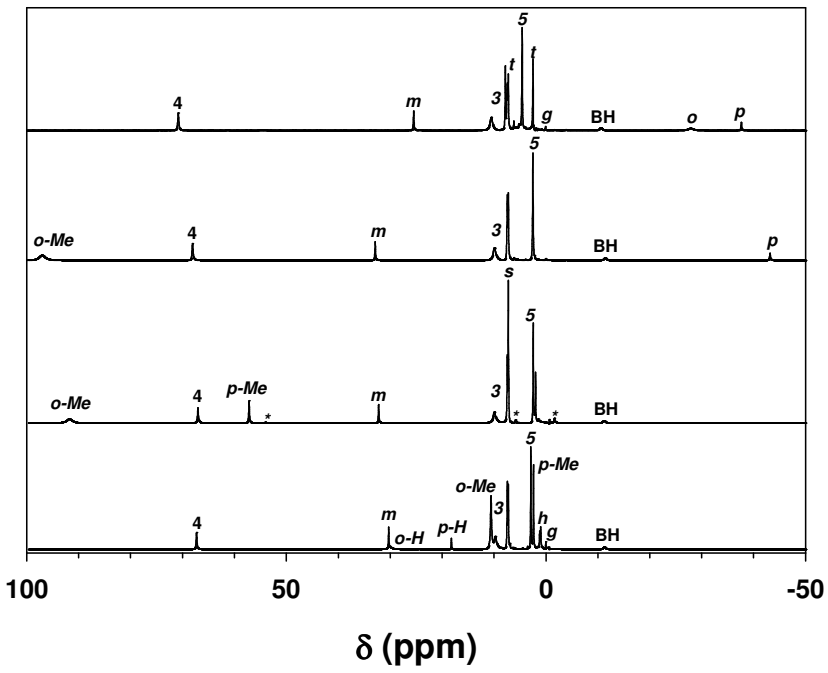

Fig. 2. ^{1}H NMR spectra (500 MHz, $CDCl_3$, 295 K) of [($Tp^{Ph,Me}$)Ni–SAr] (Ar = Ph, top; 2,6-$Me_2C_6H_3$; 2,4,6-$Me_3C_6H_2$; 2,4,6-$^{i}Pr_3C_6H_2$, bottom). The pyrazole positions are labeled 3 (Ph), 4 (H) and 5 (Me); *ortho*, *meta* and *para* arylthiolate resonances are labeled *o* (H and/or Me), *m* (H) and *p* (H and/or Me); known impurities are also labeled (*g*, silicone grease; *h*, *n*-hexane; *s*, $CHCl_3$; *t,* toluene; *, [($Tp^{Ph,Me}$)$_2$Ni]).[45,46]

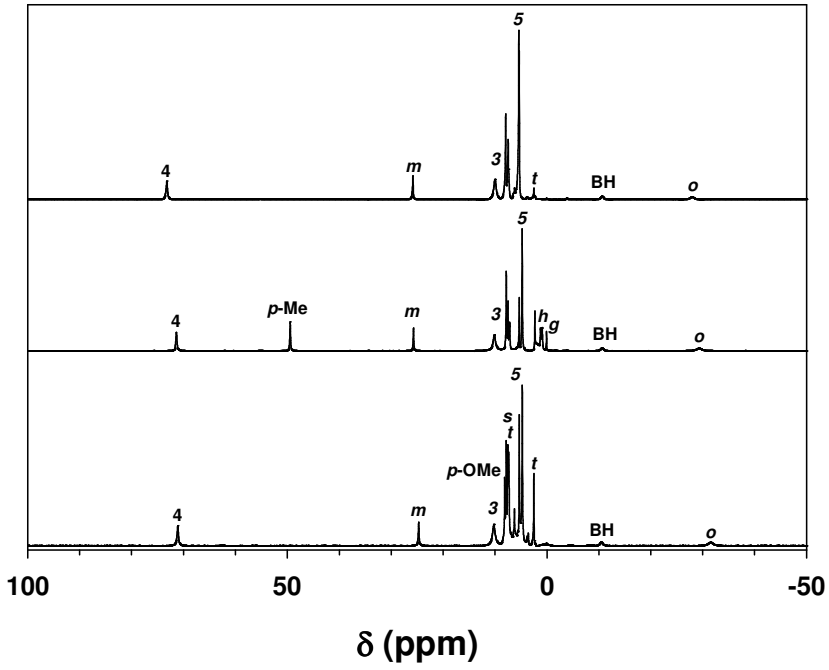

Fig. 3. ^{1}H NMR spectra (500 MHz, CD_2Cl_2, 295 K) of [($Tp^{Ph,Me}$)Ni–S–C_6H_4-4-Y] (Y = Cl, top; Me, middle; OMe, bottom). The pyrazole positions are labeled 3 (Ph), 4 (H) and 5 (Me); *ortho*, *meta* and *para* arylthiolate resonances are labeled *o* (H), *m* (H) and *p* (H or Me or OMe); known impurities are also labeled (*g*, silicone grease; *h*, *n*-hexane; *s*, $CHDCl_2$; *t,* toluene).[45]

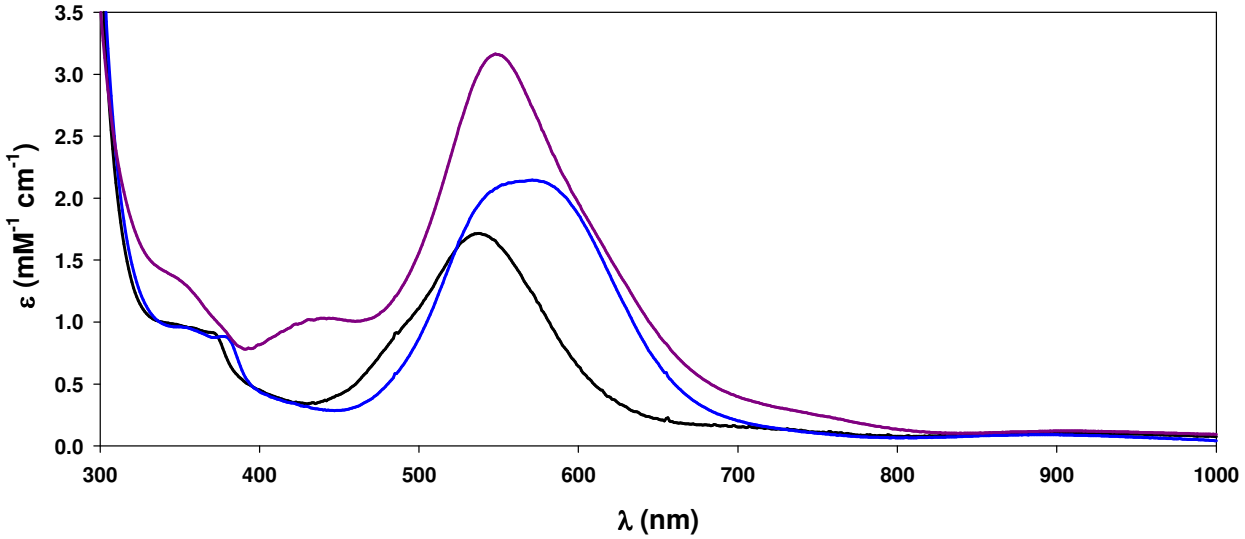

Fig. 4. UV-Vis-NIR spectra of [(Tp^{Ph,Me})Ni–S–R"$_3$C$_6$H$_2$] in CH_2Cl_2 solutions at 295 K (R" = H, black; Me, blue; ^{i}Pr, purple).

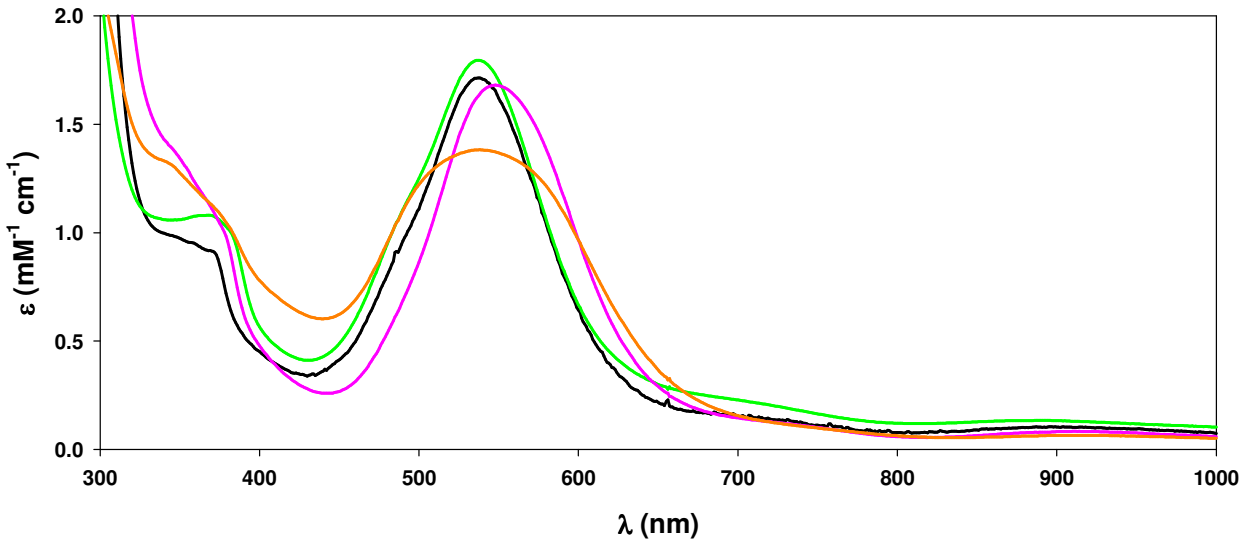

Fig. 5. UV-Vis-NIR spectra of [(Tp^{Ph,Me})Ni–S–C$_6$H$_4$-4-Y] in CH_2Cl_2 solutions at 295 K (Y = Cl, green; H, black; Me, pink; OMe, orange).

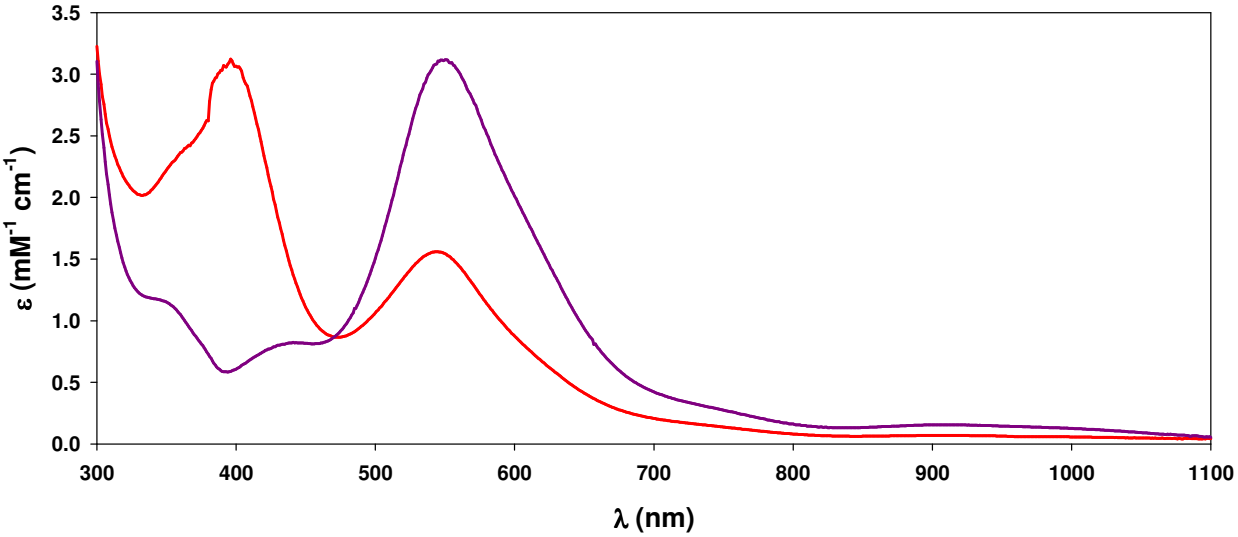

Fig. 6. Electronic spectra of [(Tp^{Ph,Me})Ni–S–2,4,6-^{i}Pr$_3$C$_6$H$_2$] in CH_2Cl_2 (purple) and CH_3CN (red) solutions at 295 K.

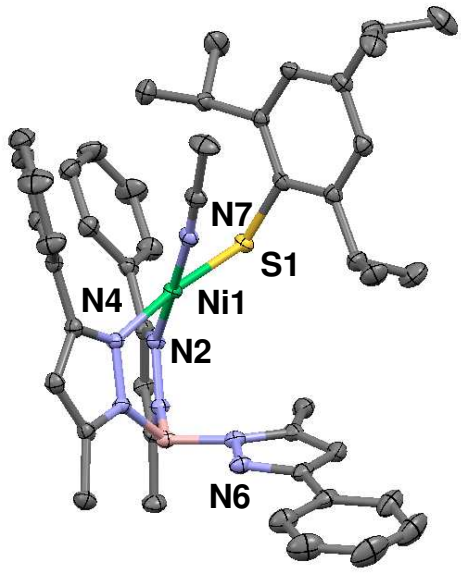

Fig. 7. Thermal ellipsoid plot (50% probability) of [(κ^2-Tp^{Ph,Me})Ni(NCMe)(S–2,4,6-^{i}Pr$_3$C$_6$H$_2$)]. Hydrogen atoms are omitted for clarity. Coordinate bond lengths (Å): Ni1–S1, 2.1954(5); Ni1–N2, 1.886(1); Ni1–N4, 1.934(1); Ni1–N7, 1.850(2); N7–C46, 1.137(2). Coordinate bond angles (°): N2–Ni1–N4, 89.06(6); N2–Ni1–N7, 177.46(6); N4–Ni1–N7, 92.48(6); N2–Ni1–S1, 87.32(4); N4–Ni1–S1, 173.29(4); N7–Ni1–S1, 91.35(5); Ni1–N7–C46, 170.7(2); N7–C46–C47, 177.3(2); Ni1–S1–C31, 111.22(6).

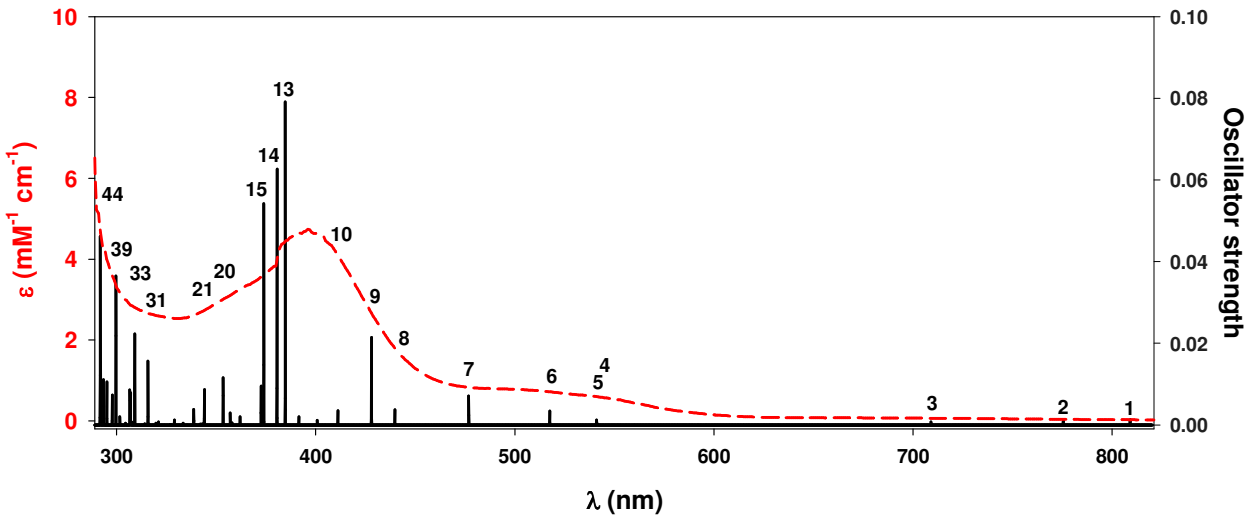

Fig. 8. Comparison of the TD-DFT calculation on a simplified [(κ^2-Tp)Ni(NCMe)(SPh)] model (right axis, black) to the extrapolated electronic spectrum of [(κ^2-Tp^{Ph,Me})Ni(NCMe)(S–2,4,6-^{i}Pr$_3$C$_6$H$_2$)] (left axis, red: $\varepsilon = [\varepsilon_{CH3CN} - 0.4 \times \varepsilon_{CH2Cl2}]/0.6$; *cf.*, Fig. 6). Significant orbital contributions to the enumerated transitions are given in the ESI (Table S2).†